ACS APPLIED ELECTRONIC MATERIALS

pubs.acs.org/acsaelm

Article

Correspondence of Plasticity and Hysteresis in Organic Electrochemical Transistor Synapses

Heyi Zhang,* Gonzalo Rivera-Sierra, and Juan Bisquert*

Cite This: *ACS Appl. Electron. Mater.* 2026, 8, 5453−5463

Read Online

ACCESS | Metrics & More | Article Recommendations | Supporting Information

ABSTRACT: Organic electrochemical transistors (OECTs) display two prominent phenomena: pronounced hysteresis in transfer curves and synaptic-like plasticity under gate-voltage pulse trains. These two observations are usually analyzed with different protocols, and the direction of transfer hysteresis (clockwise/counterclockwise, CKW/CCW) is rarely used to anticipate the polarity of pulse-driven weight updates (synaptic potentiation or depression). In the context of a minimal dynamical framework built on an internal ionic state, we show that transfer-loop orientation provides an operational indicator of the sign of pulse-induced updates once the device polarity factor, pulse protocol, and operating window are fixed. More specifically, the observable response is governed by the competition between an effective ionic relaxation time and an effective electronic readout time, both defined within a stated operating window. Changing the balance between these two effective times changes the relative weight of state lag and current readout, which can switch the loop orientation and reverse the pulse response accordingly. The result is proposed not as a universal recipe with strictly constant material parameters but as a compact interpretation framework for relating fast transfer sweeps to pulse-driven plasticity under controlled OECT operating conditions.

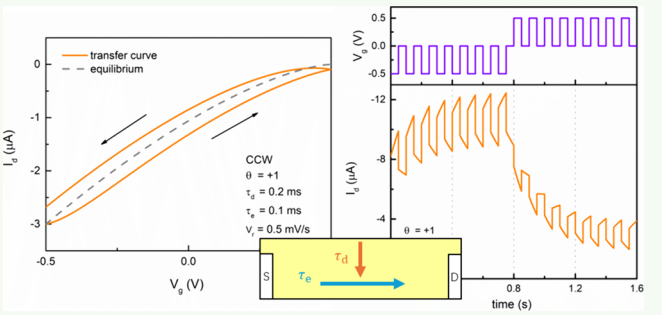

KEYWORDS: *organic electrochemical transistor, synaptic plasticity, transfer hysteresis, ionic relaxation, neuromorphic devices*

1. INTRODUCTION

Organic electrochemical transistors (OECTs) operate through the coupling of ionic motion in an electrolyte and electronic transport in an organic mixed ionic–electronic conductor (OMIEC) channel. This mechanism enables low-voltage operation, large transconductance, and intrinsically history-dependent responses, which is why OECTs have become central to bioelectronics and increasingly attractive for neuromorphic hardware. Previous reviews and analytical studies have established the physical basis of OECT operation in terms of volumetric ionic charging, chemical capacitance, and the characteristic timescales imposed by materials, geometry, and bias history.[1−7]

Two experimental signatures are routinely invoked when OECTs are discussed as artificial synapses. First, repeated gate-voltage pulses can drive progressive changes in drain-current amplitude, mimicking synaptic weight updates, short-term plasticity, or retention-like behavior.[8−14] Second, quasi-static transfer sweeps often exhibit pronounced hysteresis, usually classified by loop orientation as clockwise (CKW) or counterclockwise (CCW).[5,15−17] Although these signatures are frequently reported side by side, they are usually extracted under different protocols and interpreted in different languages: transfer hysteresis is discussed in terms of forward/backward sweep asymmetry, whereas synaptic behavior is described through pulse-to-pulse current evolution. As a result, it remains difficult to infer potentiation or depression from a rapid, standardized transfer measurement, despite the practical value that such a relation would have for screening materials and operating conditions.

Experimental OECT synapse studies have demonstrated pulse-driven potentiation/depression, short-term plasticity, paired-pulse behavior, and long-term conductance modulation in different material systems, including PEDOT:PSS OECT synapses and organic electrochemical neuromorphic devices.[8−11,18] More recent reports further show that ion-transport engineering or ion-doping kinetics can simultaneously affect transfer hysteresis, transient response, and synaptic plasticity. For example, a cross-linked polyvinyl alcohol (CX-PVA) ion-transport layer was applied to enlarge the transfer hysteresis window while

Received: April 2, 2026
Revised: June 11, 2026
Accepted: June 15, 2026
Published: June 30, 2026

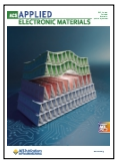

improving stronger excitatory postsynaptic current (EPSC) accumulation and paired-pulse facilitation (PPF)/prolonged long-term potentiation (LTP) behavior.[19] Annealing-modulated ion doping/dedoping kinetics was reported to tune retention, STP/LTP transition, and synaptic weight in OECTs.[20] Pulse-polarity-controlled conductance increase and decrease through electrochemical doping/dedoping have also been demonstrated in OECT arrays.[21] These studies support the physical premise that transfer hysteresis and pulse-driven plasticity are both governed by delayed ionic–electronic coupling. However, they do not explicitly formulate transfer-loop orientation as an operating-window indicator for pulse-update polarity under a fixed polarity convention.

The central point of this work is that hysteresis direction and plasticity polarity are not independent empirical labels. Rather, both are dynamical manifestations of the same internal state evolving across characteristic timescales. The Bernards–Malliaras framework established that OECT transients can be described through coupled ionic and electronic processes, providing a compact bridge between steady-state and transient response.[22] More recent diffusion–transport treatments have clarified how ionic relaxation and electronic readout jointly determine switching behavior and scan-rate-dependent hysteresis, making it possible to discuss transfer loops, pulse transients, and relaxation within a common timescale picture.[16,23−25]

At the same time, many demonstrations of OECT-based synaptic behavior show strong dependence on pulse timing, operating point, and device geometry.[8−10,23,26] This practical sensitivity matters because neuromorphic benchmarking is often time-consuming, whereas transfer measurements are comparatively rapid and reproducible. A predictive relation between loop orientation and pulse-update polarity would do more than clarify interpretation: it would provide a compact screening logic for device comparison and protocol design.[18,27,28] However, logic must be framed carefully because the effective transport parameters that set the response can themselves vary with bias and state.

Here, we establish a protocol-consistent correspondence between CKW/CCW transfer hysteresis and depression/potentiation in OECT synaptic protocols within a minimal diffusion–transport model parameterized by three physically transparent quantities: the ionic relaxation/diffusion time τ_d, the electronic readout (transit) time τ_e, and a polarity factor θ aligned with the intrinsic operating polarity of the device under the adopted drain bias V_{ds}, consistent with recent analytical diffusion–transport treatments.[16,24,25] More specifically, the aim is not only to show that hysteresis and plasticity can coexist but also to state when their correspondence becomes operationally well-defined.

Within this framework, θ determines how the delayed internal state is projected into the measured drain current, while the pulse baseline and polarity determine which equilibrium-state increment is sampled during stimulation. The same framework also explains stimulus-level reversibility: changing the pulse baseline or polarity can reverse the apparent update polarity without changing the underlying hysteresis mechanism.

We also make explicit the scope of this reduction: in real devices, mobility, ionic diffusivity, and chemical-capacitance contributions may evolve with bias, concentration, and microstructure, so the characteristic times used here should be interpreted as effective parameters for a defined operating regime rather than universal constants. Under that restriction, the model is sufficient to organize when loop orientation can be used to anticipate pulse-update polarity and when the stimulus itself can reprogram the same device.

2. MODEL AND CONVENTIONS

For each simulated condition, the OECT is considered under a fixed drain–source bias V_{ds} and driven by a gate stimulus V_g. Following the reduced diffusion–transport picture, the channel is described by a single internal state variable A, which relaxes toward its gate-dependent equilibrium value A_{eq}.[16,24,25] In this work, A is treated as a charge-density state variable representing the average ionic occupation of the channel. By electroneutrality, the density of mobile carriers is the same. The derivative dA/dt represents the rate at which ion insertion/extraction drives the channel toward the gate-defined equilibrium manifold. This state equation is the common starting point for both transfer sweeps and pulse protocols.

The reduced model is organized by two characteristic times. The ionic relaxation (diffusion) time τ_d controls how rapidly the internal state approaches A_{eq}, while the electronic transit time τ_e controls how the instantaneous state is projected into the measured drain current. The experimentally observed hysteresis does not follow from τ_d or τ_e in isolation, but from the competition between delayed state build-up and its electronic readout. In Appendix 1, eqs (5) to (11) provide the corresponding decomposition showing how this competition enters the measured current through the delayed state and relaxation-related terms. This is the key organizing principle used below to connect loop orientation with pulse-update polarity. The ionic relaxation (diffusion) time

$$\tau_d = \frac{d^2}{D_{ion}} \tag{1}$$

sets the timescale for vertical ion penetration across a film of thickness d. D_{ion} is the ionic diffusion coefficient. While the electronic transit time

$$\tau_e = \frac{L^2}{\mu_p |V_{ds}|} \tag{2}$$

describes lateral electronic equilibration along a channel of length L, where μ_p is the effective carrier mobility. The drain-bias polarity is captured by

$$\theta = \frac{V_{ds}}{|V_{ds}|} = \pm 1 \tag{3}$$

which distinguishes the two intrinsic operating polarities considered here and fixes the sign of the measured drain-current response under the adopted drain bias. The delayed evolution of A is the physical origin of memory in the model. The role of θ is not to introduce a different state dynamic, but to specify how this same delayed state is projected into the measured drain current under the adopted drain-bias polarity and current-sign convention.

These scalings are practically useful because τ_e mainly follows a drain-bias-controlled electronic readout, whereas τ_d mainly follows thickness-controlled ionic relaxation. At the same time, the underlying mobility, ionic diffusivity, and chemical-capacitance landscape may vary with state, bias, and

https://doi.org/10.1021/acsaelm.6c00658
ACS Appl. Electron. Mater. 2026, 8, 5453−5463

microstructure. Accordingly, τ_e and τ_d are used here as effective parameters of the selected operating window rather than as strictly bias-independent constants. The constant-timescale treatment allows hysteresis and pulse protocols to be compared under the same parameter set. Meanwhile, the effective timescale can be estimated from real devices: τ_d can be obtained from ionic charging measurements, such as gate-current transients, chronoamperometry, impedance spectroscopy, or thickness-dependent charging, whereas τ_e can be estimated from channel geometry, drain bias, mobility, and drain-current readout dynamics, as detailed in Appendix 1.

The qualitative model is formulated as eqs (9) and (10), giving the derivation of the reduced state equation and drain-current expression. In the main text, we use the resulting current decomposition to interpret the transfer and pulse responses. The drain current can then be written as the sum of an electronic readout term proportional to A and a relaxation term proportional to $A_{eq}(u) - A$.

$$I_d(u, A) = -\theta \frac{qL}{\tau_e} A - qLf \frac{A_{eq}(u) - A}{\tau_d} \quad (4)$$

Separating the current in this way makes the competition explicit: the first contribution reports the accumulated state itself, whereas the second reports the residual mismatch between the instantaneous state and its gate-defined equilibrium. Depending on θ and on the relative weight of these two terms, the same state evolution can be read out as CKW or CCW transfer hysteresis and as potentiation or depression under pulsed driving.

The decomposition is especially useful because, using the state equation above, the relaxation term may also be read as proportional to dA/dt, eq 10. The measured current, therefore, contains one part linked to the state itself and another linked to the rate of state change. For a fixed θ, the observed CKW/CCW loop orientation follows from how these two contributions are combined in the forward and backward sweep branches. Changing θ reverses the sign with which the same delayed state is projected into I_d, which is why the same underlying state evolution can be assigned to different loop orientations under opposite polarity conventions. The explicit functional form of $A_{eq}(u)$ used in the simulations is given in Appendix 1. The partition factor f weights the relaxation-related contribution to the measured current. $f = 0.5$ is used here as a symmetric reference value for the relaxation-current partition, while recent work shows that f is experimentally measurable and operating-condition dependent. Simulation parameters are summarized in Table 1.

Table 1. Parameters of the Transistor[a]

sweep rate (transfer)	V_r	0.20, 0.50 mV s^{-1}
channel length	L	50 μm
partition factor	f	0.5
thermal voltage	k_BT	0.026 V

[a] τ_d and τ_e are effective operating-window descriptors, not universal device constants. The listed values are used to compare response regimes.

3. RESULTS AND DISCUSSION

3.1. Protocol Definitions

To make the correspondence between transfer hysteresis and pulse-driven plasticity explicit, we start from controlled simulations in which the polarity definition and the minimal model parameters are fixed, and only the relative balance between the relevant timescales is varied. All results shown in Figures 1–5 are obtained by simulation. Before turning to the individual cases, the essential rule is as follows: for a fixed θ and pulse convention, the observed response is governed by the competition between effective ionic relaxation (τ_d) and electronic readout (τ_e). When this competition changes sign in the measured current, the transfer-loop orientation and the pulse-update polarity change together. Stating this organizing principle here makes the case-by-case results below easier to read.

We consider two standard protocols. The first is the I_d transfer curve, obtained from a sweep of V_g (equivalently u) from u_{min} to u_{max} (forward) and back u_{max} to u_{min} (backward) at constant sweep rate V_r. A finite τd produces a lag between A and A_{eq}, which separates the forward and backward branches in the I_d–V_g plane. The second is the synaptic pulse protocol, consisting of a pulse train between V_{base} and V_{pulse}. In the main simulations, a regular square-pulse train is used, with equal pulse width and inter-pulse interval, ($t_p = \Delta t$). Here, t_p denotes the pulse-on duration, while Δt denotes the recovery interval between consecutive pulses. The readout is taken at the same fixed time point within each pulse, so that the reported pulse envelope reflects the accumulated state reached after the same stimulation time in every cycle. Potentiation and depression are classified from the pulse-to-pulse evolution of the readout-current magnitude $|I_d|$ at this fixed readout point. An increase in $|I_d|$ from pulse to pulse is defined as potentiation, whereas a decrease in $|I_d|$ is defined as depression. If the interval is not long compared with τ_d, the state A does not fully recover to the baseline equilibrium between pulses, and the pulse-to-pulse envelope drifts cumulatively.

This polarity dependence is visualized in Figure 1c. For $\theta = -1$, the transfer loops (green traces) appear in the positive I_d half-plane, whereas the $\theta = +1$ loops (blue traces) are mirrored into the negative I_d half-plane relative to the $I_d = 0$ baseline. In this sense, changing θ primarily reverses the intrinsic operating polarity with which the same state dynamics are projected onto the measured current, without introducing a different hysteresis mechanism. Figure 1c also shows the expected sweep-rate dependence: when the sweep rate increases from $V_r = 0.2$ to 0.5 mV/s (lighter to darker traces within each θ), the forward and backward branches separate more strongly, and the hysteresis opening becomes larger.

Operational definitions used throughout are as follows. CKW/CCW denotes the clockwise or counterclockwise direction traced in the I_d–V_g plane when the system is traversed forward and then backward, as indicated by the arrows in each transfer plot. Potentiation/depression is defined, under a fixed θ, by the pulse-to-pulse evolution of the readout magnitude: potentiation corresponds to a monotonic increase in the envelope magnitude, whereas depression corresponds to a monotonic decrease. Because the sign of I_d depends on θ, we report both the signed current and $|I_d|$ where appropriate to avoid ambiguity.

https://doi.org/10.1021/acsaelm.6c00658
ACS Appl. Electron. Mater. 2026, 8, 5453−5463

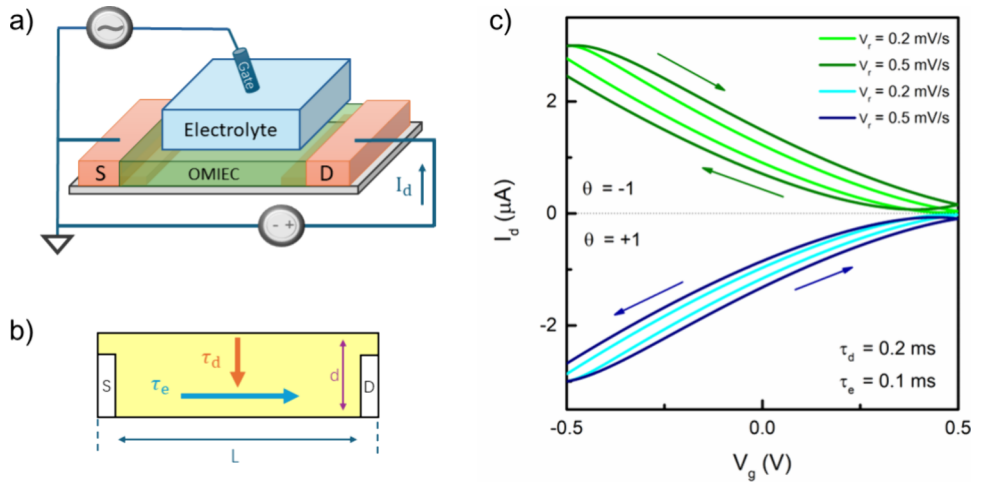

Figure 1. (a) OECT schematic. (b) Reduced diffusion–transport picture with timescales. (c) Example transfer curves simulated for two sweep rates (light/dark) under both θ = −1 and θ = +1 with arrows indicating sweep direction. The arrows indicate the forward and backward sweep directions used to define the loop orientation. CKW and CCW denote clockwise and counterclockwise trajectories. Parameters are as labeled and listed in Table 1.

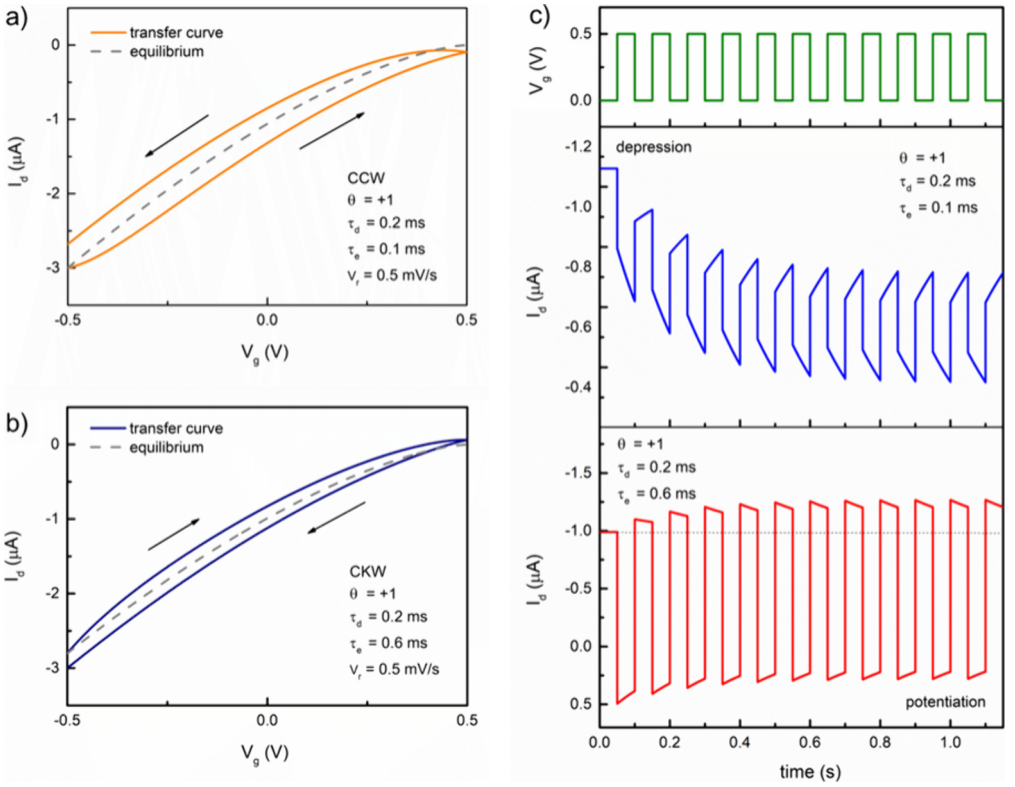

Figure 2. Corresponding results for θ = +1 under a fixed positive-going pulse protocol. (a) Simulated CCW transfer loop for the smaller effective electronic readout time τ_e = 0.1 ms (orange), with τ_d kept fixed; (b) simulated CKW transfer loop obtained when τ_e = 0.6 ms (blue) is increased while the sweep protocol and τ_d are kept unchanged. The dashed gray curve in (a,b) is the equilibrium reference obtained when the internal state follows A_{eq} without delay. Arrows indicate the forward and backward sweep directions; (c) Gate-voltage pulse train between the baseline and pulse levels shown in green, together with the corresponding drain-current responses. Potentiation and depression are classified from the pulse-to-pulse evolution of the readout-current magnitude $|I_d|$ at the fixed readout point within each pulse: an increasing envelope is defined as potentiation, whereas a decreasing envelope is defined as depression. Parameters are as labeled.

https://doi.org/10.1021/acsaelm.6c00658
ACS Appl. Electron. Mater. 2026, 8, 5453−5463

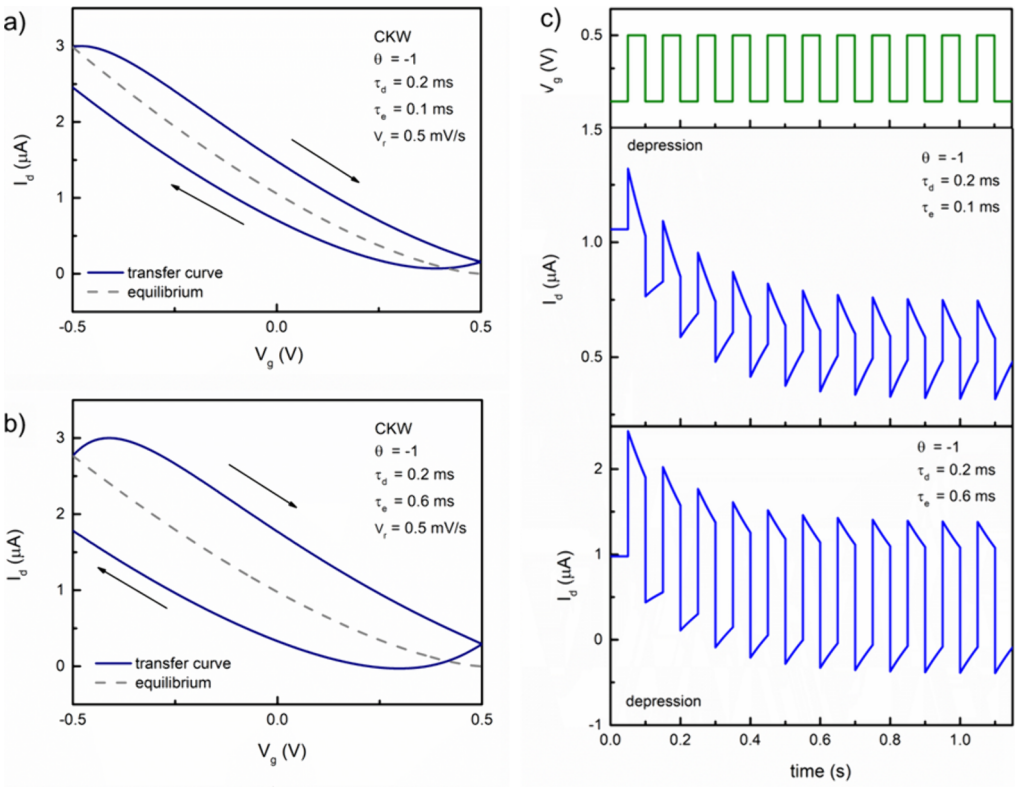

Figure 3. $\theta = -1$ situation: (a) CKW transfer loop for $\tau_e = 0.1$ ms (blue); (b) CKW transfer loop for $\tau_e = 0.6$ ms (blue). (c) Pulse gate voltage train between 0 and +0.5 V (green) and the corresponding $I_d(t)$: depression for $\tau_e = 0.1$ ms (blue) and $\tau_e = 0.6$ ms (red). The dashed gray curve is the equilibrium reference. Parameters are as labeled.

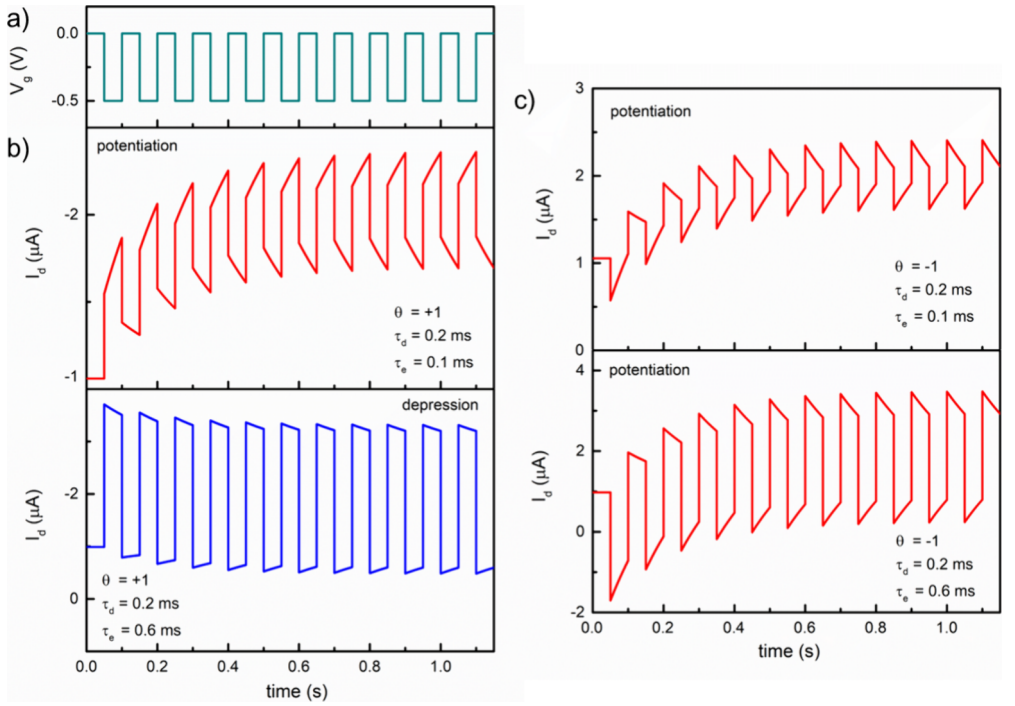

Figure 4. Stimulus-level inversion by changing the pulse baseline/polarity. Relative to the positive-going pulse protocol used in Figures 2 and 3, the pulse waveform is shifted to a negative-going sequence, while the effective device parameters τ_d and τ_e, the polarity setting θ is the same. (a) Gate-voltage pulse train $V_g(t)$ used in the synaptic protocol. (b) Pulse-driven drain-current responses for $\theta = +1$ at fixed $\tau_d = 0.2$ ms, showing potentiation (red, $\tau_e = 0.1$ ms) vs depression (blue, $\tau_e = 0.6$ ms). (c) Pulse-driven drain-current responses for $\theta = -1$ with the same τ_d and τ_e, illustrating that the observed update polarity is constrained by the readout convention and the stimulus, while τ_e primarily reshapes the readout dynamics.

https://doi.org/10.1021/acsaelm.6c00658
ACS Appl. Electron. Mater. 2026, 8, 5453−5463

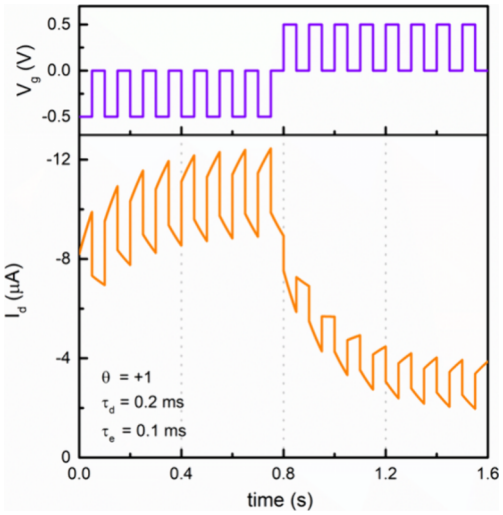

Figure 5. Complete switching example simulated under pulse-baseline reversal within one continuous pulse train. The gate-voltage sequence switches mid-train from negative pulses (0 ↔ –0.5 V) to positive pulses (0 ↔ +0.5 V) under fixed θ, while the same effective parameters τ_d and τ_e set is as labeled. The drain-current response shows a corresponding inversion of the pulse-to-pulse update trend, demonstrating that the same reduced device state dynamics can be read out as opposite cumulative updates when the stimulus baseline/polarity is changed.

Before discussing individual cases, it is useful to state the organizing principle explicitly. The equations used for these simulations are summarized in Appendix 1, and here we focus on how the resulting delayed-state dynamics appear under transfer-sweep and pulse-train protocols. For a fixed polarity convention θ and a stated pulse waveform, the transfer loop and the pulse train are two measurements of the same delayed internal-state dynamics $A(t)$. The observed CKW/CCW orientation is set by how ionic-state lag, governed by the effective τ_d, is projected into the drain-current readout through the effective electronic timescale τe and the sign factor θ. The same competition, therefore, controls whether the pulse envelope evolves as potentiation or depression.

Once θ and the pulse sign/baseline are specified, the loop orientation is associated with the sign of the cumulative update under the corresponding protocol. Reversing θ reverses the sign with which the internal-state evolution is projected into I_d, so the CKW/CCW assignment associated with a given τ_d–τ_e competition is correspondingly exchanged. Reversing the pulse baseline or pulse polarity does not create a new hysteresis mechanism; it merely changes the sampled current increment and can therefore invert the apparent potentiation/depression outcome.

3.2. Correspondence of Transfer Hysteresis and under Polarity θ = +1

Figure 2 establishes the central result for the device polarity setting θ = +1. We first examine the transfer loops. In Figure 2a (orange), $\tau_d = 0.2$ ms while $\tau_e = 0.1$ ms ($\tau_d > \tau_e$). The forward and backward sweeps (arrow pointing) form a CCW loop around the gray dashed equilibrium curve, reflecting nonequilibrium state lag during the finite-rate scan. In Figure 2b (blue), τ_d and the sweep protocol (V_r) are kept unchanged, but τ_e is increased to 0.6 ms, the ordering of the two branches reverses ($\tau_e > \tau_d$) and the loop becomes CKW. Thus, under θ = +1, changing the electronic readout time can invert the observed loop orientation even when the ionic relaxation time is held fixed.

We next apply a pulse train using the same parameter sets as shown in Figure 2c. The top panel shows the gate stimulus (green), consisting of square pulses between V_{base} (0 V) and V_{high} (0.5 V). For the CCW case with smaller τ_e, the drain-current spikes (blue) progressively shrink in magnitude, and the readout current at a fixed point within each pulse drifts toward smaller $|I_d|$, which we classify as depression. In contrast, for the CKW case with larger τ_e (0.6 ms), the spike envelope (red) grows pulse to pulse, meaning that $|I_d|$ increases, which is classified as potentiation. Under the same device polarity and the same stimulus, the orientation of the transfer loop indicates the sign of the synaptic update.

This protocol-consistent mapping means that the transfer loop and the pulse response are two projections of the same internal state measured under two different waveforms. Having established the correspondence for θ = +1, we next consider how strongly it is constrained by device polarity and by the relative magnitude of the effective timescales.

Stated differently, the correspondence becomes operationally defined only after the device polarity θ and the pulse waveform are fixed: within that defined operating convention, the transfer-loop orientation is consistently associated with the sign of the pulse-driven cumulative update.

Taken together, the key observation is that, for a fixed device polarity θ, the loop orientation in transfer within the selected operating window indicates the sign of the pulse envelope. When the transfer loop is CCW, the pulse train yields a monotonic drift consistent with depression. When the loop switches to CKW, the pulse response reverses accordingly and becomes potentiative under the same readout convention. Within the reduced model, loop orientation, therefore, serves as a compact proxy for the sign of cumulative updates under a matched protocol.

This correspondence is not a naming coincidence. Both observables originate from the same state lag: loop orientation reports how A is displaced from A_{eq} on the forward and backward branches, while the pulse envelope reports whether successive pulses sample progressively larger or smaller departures from equilibrium. Accordingly, the apparently dominant timescale depends on how the delayed state is read out: τ_d dominates when state lag is the main source of memory, whereas τ_e dominates when the same lag is projected with opposite sign or weight into I_d.

Moreover, Figure 2 shows that the correspondence does not rely on a unique operating point. It survives across more than one parameter set and therefore points to a practical use: loop orientation and envelope drift are both robust observables that can be extracted rapidly, allowing transfer sweeps to serve as an efficient screening metric before more time-consuming pulse benchmarking.

3.3. Polarity (θ) Constraint under θ = –1

Figure 3 repeats the same analysis with the device polarity reversed (θ = –1) while keeping τ_d, τ_e, V_r, and the stimulus definitions unchanged. The transfer loops shown in Figure 3a,b remain hysteretic, but now both parameter sets produce clockwise (CKW) loops around the grey dashed equilibrium trace. The arrows again indicate the forward and backward sweep

https://doi.org/10.1021/acsaelm.6c00658
ACS Appl. Electron. Mater. 2026, 8, 5453–5463

directions. Reversing θ, therefore, changes the sign of I_d through the intrinsic operating polarity of the device but does not alter the underlying state lag responsible for hysteresis.

Figure 3 isolates the role of the device-polarity factor θ. Once θ is fixed at −1, varying τ_e within the range considered does not reverse the orientation of the transfer loop: the forward and backward branches remain ordered in the same CKW sense for both the fast-readout and slow-readout cases. This polarity constraint arises from the sign structure of the current expression, reversing θ reverses the electronic readout term but not the relaxation-related term, so the two contributions reinforce rather than compensate each other for θ = −1 within the explored parameter range. In other words, τ_e still reshapes the transient readout, but under this polarity convention, it does not overturn the qualitative loop sense produced by the state projection.

The practical reading rule is therefore θ-dependent. Under θ = +1 and under the positive-pulse protocol analyzed in Figure 2, CCW corresponds to depression, whereas CKW corresponds to potentiation. Under θ = −1 and the positive-pulse protocol analyzed in Figure 3, the explored parameter sets remain CKW and correspond to depression. The transfer-to-pulse relation is thus predictive only when θ and the stimulus sign are stated explicitly.

This invariance is precisely what makes hysteresis direction operationally useful. Once the loop orientation has been established from a rapid transfer measurement under a given V_{ds} (hence a given θ), the corresponding pulse-response tendency is constrained within the same operating window. The mapping should, therefore, be read as an organizing correspondence within the stated convention, not as a claim that any single transfer curve universally determines plasticity under arbitrary bias history.

This comparison also clarifies what can and cannot change the update polarity. In the present framework, varying τe reshapes the readout dynamics but does not provide a stimulus-level lever for inverting the direction of cumulative updates under a fixed protocol. To reverse potentiation and depression without changing the device polarity, the stimulus baseline or pulse polarity must be changed so that the sampled equilibrium-state increment changes sign.

In addition, the transfer-to-pulse mapping requires incomplete recovery between pulses. If the inter-pulse interval Δt becomes much longer than τd, when $\Delta t \gg \tau_d$, the internal state relaxes close to equilibrium between pulses, cumulative drift largely vanishes, and the apparent potentiation/depression becomes weak even if hysteresis is still visible in transfer. This long-interval limit is illustrated in Figure S1. In this long-interval limit, pulse-to-pulse accumulation is suppressed because A nearly recovers to $A_{eq}(V_{base})$ before each pulse. The transfer hysteresis can nevertheless remain visible under a finite scan rate because, during a continuous sweep, A lags behind the continuously changing $A_{eq}(V_g)$.

3.4. Stimulus-Level Inversion via Baseline/Polarity

We now show how the established correspondence can be used operationally. The plasticity polarity can be reversed without changing the device by changing only the stimulus baseline or pulse polarity, while keeping τ_d, τ_e, θ, V_{ds}, and the device structure fixed. In Figure 4a, the pulse train is shifted from 0 ↔ +0.5 V sequence used in Figures 2 and 3 to a negative-going 0 ↔ −0.5 V sequence. This does not alter the underlying hysteresis mechanism; instead, it changes the sign of the equilibrium-state increment sampled during each pulse and, therefore, reverses the cumulative update direction. When the transfer–pulse relation is established, stimulus-level inversion follows because the pulse sequence samples the same device dynamics around a different baseline.

Figure 4b (θ = +1) compares two electronic readout times at fixed ionic relaxation τ_d = 0.2 ms. Under the negative-pulse waveform, the τ_e = 0.1 ms trace (red) shows potentiation, with the pulse-to-pulse envelope increasing in $|I_d|$, whereas the τ_e = 0.6 ms trace (blue) shows depression, with a decaying $|I_d|$ envelope. Figure 4c (θ = −1) shows the corresponding responses under the opposite device-polarity convention. In that case, both traces follow the polarity constraint discussed above, so the waveform change alone does not generate the same inversion seen for θ = +1.

Additional comparisons obtained by varying τ_d are provided in Figures S3 and S4. These results show that changing the effective ionic relaxation time mainly modulates the degree of lag and the strength of cumulative updates, without overturning the central correspondence identified above. In this way, the Supporting Information extends the interpretation across additional τ_d values rather than introducing a separate mechanism.

Table 2 summarizes the representative cases under positive and negative-going pulses gate stimulus discussed in this work, which shows the associated hysteresis sense and pulse-response within the reduced framework.

The key point is that CKW and CCW are not globally tied to potentiation or depression in isolation. The correspondence is operationally defined only within a stated polarity convention, pulse protocol, and operating window, which is why θ and waveform sign must accompany any use of hysteresis direction as a readout indicator.

The stimulus-level inversion shown in Figure 4 changes the equilibrium state sampled during each pulse by changing the pulse baseline or polarity. Pulse timing provides a related but distinct control. Although the main simulations use a regular protocol with $t_p = \Delta t$, these two quantities correspond to different parts of the state evolution. During the pulse-on period of width t_p, A evolves toward $A_{eq}(V_{pulse})$, whereas during the inter-pulse interval Δt, it relaxes toward $A_{eq}(V_{base})$. Thus, t_p controls the state displacement during stimulation, while Δt controls residual-state recovery before the next pulse. As shown in Figure S5, for the negative-going potentiating protocol with $\Delta t = 0.1\tau_d$, increasing t_p from 0.5 τ_d to 3 τ_d changes the magnitude and rate of potentiation within the same delayed-state mechanism. Paired-pulse and rate-dependent effects can be interpreted similarly as incomplete recovery and residual-state accumulation, although their full quantitative mapping is beyond the scope of this work.

3.5. Complete Switching under Pulse-Baseline Reversal

Finally, Figure 5 closes the results section with a complete switching example in which the pulse baseline is reversed mid-train while the device parameters remain fixed. Starting from a transfer measurement, the loop orientation provides a rapid operational indicator of the pulse-driven update tendency under a fixed θ, while a shift in baseline or pulse polarity provides a practical way to switch between weight increase and weight decrease without modifying the device itself.[14,27,29−31]

The gate-voltage train in Figure 5 is composed of two consecutive pulse segments under fixed device parameters as

https://doi.org/10.1021/acsaelm.6c00658
ACS Appl. Electron. Mater. 2026, 8, 5453−5463

Table 2. Summary of the Transfer-to-Pulse Correspondence with Applied Gate-Voltage Pulses[a]

polarity setting	effective regime	transfer hysteresis	positive-going pulse	negative-going pulse
θ=+1	smaller τ_e/fast electronic readout	CCW	depression	potentiation
θ=+1	bigger τ_e/slow electronic readout	CKW	potentiation	depression
θ=−1	smaller τ_e/fast electronic readout	CKW	depression	potentiation
θ=−1	bigger τ_e/slow electronic readout	CKW	depression	potentiation

[a]Here τ_e is varied to represent different effective electronic readout regimes, while τ_d is kept fixed within the selected operating window. The response polarity is defined from the pulse-to-pulse evolution of the readout-current magnitude $|I_d|$ under the stated pulse protocol.

labeled, and the drain current responds with a clear inversion of the pulse-to-pulse trend when the pulse polarity is reversed. Additional comparisons are provided in Figure S2, including the cases in which τ_d is varied. Thus, the switching experiment does not stand apart from the earlier figures; rather, it condenses the same transfer-to-pulse logic into a single continuous protocol. Although the main analysis is based on numerical simulations, a representative experimental comparison is provided in Figure S6, showing that the apparent pulse-update polarity of the same OECT device can be changed by the drain-bias/readout condition under the same gate-pulse protocol. The experimental methods are described in Appendix 2.

Operationally, transfer-loop orientation can guide the choice of pulse conditions within a known polarity convention and operating window, while pulse-baseline reversal provides a direct way to switch the apparent update direction.

The present single-state model neglects additional retention processes such as interfacial trapping, ion trapping, multiple ionic species, or slow structural relaxation. Such effects may be important in long-memory OECT synapses and could shift the transfer-to-pulse correspondence. The present result should be read as a reduced operating-window rule for the dominant delayed ionic state A, not as a complete model of strongly trapped devices.

4. CONCLUSIONS

This work links two signatures that are often reported side by side in OECT neuromorphic studies but are rarely interpreted within a single, protocol-consistent framework. Within a minimal diffusion–transport model, we establish a correspondence between the orientation of transfer hysteresis (CKW/CCW) and the sign of pulse-driven updates (potentiation/depression), provided that the device polarity θ is stated explicitly. The mapping originates from the interplay between ionic relaxation and electronic readout, captured here through the effective characteristic times τ_d and τ_e, which jointly determine the state lag and its projection onto the measured drain current.

At the same time, the analysis clarifies an equally important practical point: update polarity is not determined by device physics alone but can be reprogrammed at the stimulus level. By shifting the pulse baseline or pulse polarity, the sign of the equilibrium-state increment sampled by the protocol is reversed, so that cumulative updates invert even though the underlying hysteresis mechanism remains unchanged. Transfer hysteresis can serve as both a descriptive signature and a compact operating-window indicator of synaptic update polarity under a known polarity convention and pulse protocol. This correspondence should be interpreted as an operating window rule of the reduced model. In real OECTs, bias-dependent mobility, ionic diffusivity, chemical capacitance, carrier density, trapping, and morphology may shift the quantitative boundaries between regimes, although the central interpretation in terms of delayed internal-state dynamics remains applicable.

APPENDIX 1

We describe the OECT switching dynamics with a single internal ionic state variable A, defined as the spatially averaged inserted ionic concentration in the channel film, a concentration-like state variable consistent with the reduced diffusion–transport model used throughout this work.[16,24,25] A timescale picture is adopted where τe is interpreted mainly through drain-bias-controlled electronic readout and τd mainly through thickness-controlled ionic relaxation. This is a practical operating-window approximation, not a claim that real devices always exhibit a unique one-to-one dependence of τ_e on V_{ds} or of τ_e on thickness alone.

Under a given effective gate potential u, the channel tends toward an equilibrium state $A_{eq}(u)$ determined by the gate-dependent thermodynamics (chemical capacitance/density of states). In the simulations of this work, we use the following functional form for $A_{eq}(u)$ which corresponds to the density of states used for holes and, by electroneutrality, also applies to ions:

$$A_{eq}(u_g) = \frac{2}{3} A_0 \left[\frac{q(u_v - u_g)}{k_B T}\right]^{\frac{3}{2}} \tag{5}$$

Here, k_B is the Boltzmann's constant, T is the absolute temperature, u_V is the valence edge potential, and the A_0 is a density per length. This expression follows the DOS-based equilibrium manifold used in the switching treatment and provides the thermodynamic relation between the gate stimulus and the equilibrium ionic state.

$$g_a(qu_g) = -\frac{dA_{eq}}{d(qu_g)} = \frac{A_0}{k_B T}\left[\frac{q(u_v - u_g)}{k_B T}\right]^{\frac{1}{2}} \tag{6}$$

$$C_\mu = -q\frac{dA_{eq}}{du_g} \tag{7}$$

The chemical capacitance C_μ, therefore, fixes the local thermodynamic slope of the equilibrium state. In the more general transient formulation, it couples naturally to ionic transport, so

https://doi.org/10.1021/acsaelm.6c00658
ACS Appl. Electron. Mater. 2026, 8, 5453−5463

that the vertical diffusion resistance may be written as,

$$R_d = \frac{\tau_d}{C_\mu} \tag{8}$$

which makes explicit that the experimentally observed relaxation can depend not only on diffusion length and diffusivity but also on the state-dependent storage response of the mixed conductor. In other words, even before additional nonidealities are invoked, the effective ionic timescale extracted from experiment need not map onto a single bias-independent D_{ion}.

The minimal transient diffusion–transport model used as the starting point for the present analysis is as follows:

$$I_d(u, A) = -\theta \frac{qL}{\tau_e} A - qLf \frac{dA}{dt} \tag{9}$$

$$\tau_d \frac{dA}{dt} = A_{eq}(u) - A \tag{10}$$

Here, L is the channel length, q is the elementary charge, f is a dimensionless partition factor used in the reduced form, and τ_e is an electronic time constant controlling the lateral electronic equilibration/readout. In a more microscopic description, τ_e inherits contributions from carrier mobility, carrier density, and state-dependent conductivity; in this work, it is used as an effective readout timescale over the operating window considered.

The dimensionless factor f describes how the relaxation-related current contribution is partitioned into the measured terminal current. We use $f = 0.5$ as a symmetric reference value, following the minimal reduced OECT switching model, corresponding to a case where the gate-induced relaxation current is not strongly biased toward one terminal. Recent experimental work has shown that f can be estimated from high-frequency source and gate current amplitudes, $f = |I_{S,AC}|/|I_{G,AC}|$, and that it depends on operating and device conditions.[32] Therefore, f is an effective operating-condition-dependent factor. In this work, fixing $f = 0.5$ keeps the analysis focused on the roles of τ_d, τ_e, and θ. Varying f would shift the quantitative boundary without introducing a different delayed-state mechanism.

For a linear sweep $u(t)$ at a constant sweep rate $V_r = du/dt$, the internal state follows

$$\tau_d V_r \frac{dA}{du} = A_{eq}(u) - A \tag{11}$$

Here, τ_d is the ionic relaxation (diffusion) time constant that controls the lag of A behind $A_{eq}(u)$ during a finite-rate sweep. Under a transfer curve measurement, the gate overdrive $u(t)$ is imposed as a linear ramp on the forward branch and as the corresponding reverse ramp on the backward branch. The observed loop orientation, therefore, reflects the branch ordering produced when the delayed state $A(t)$ is projected onto the measured current through the drain-current expression below. Because μ_p, C_μ, and the local transport coefficients may all vary with state, the τ_d entering the reduced sweep equation should likewise be interpreted as an effective parameter for the selected bias window.

The drain current can be expressed as the sum of an electronic readout term proportional to A and a relaxation term proportional to the state mismatch $A_{eq} - A$, eq (4). The polarity factor θ is treated here as a device-level polarity parameter associated with the adopted drain bias and the sign of the dominant carrier response. Using the state equation, the relaxation contribution may also be read as proportional to dA/dt, so the measured current contains one term linked to the state itself and another linked to the rate of state change. For a fixed θ, the transfer curve and the pulse response are therefore two protocol-dependent projections of the same underlying state dynamics.

The pulse protocol used in the main text can be written in the same notation by defining $u(t)$ as a piecewise-constant waveform that alternates between a baseline level and a pulse level. In that case, potentiation or depression is determined by the sign of the cumulative pulse-to-pulse drift of the readout magnitude. Equivalently, one may view the pulse response as reporting the sign of the cycle-averaged state increment over one pulse period relative to the baseline state.

This makes explicit why the transfer and pulse measurements can be compared within one framework: both are generated by the same state equation, but under different driving waveforms. The transfer loop reports how finite-rate lag orders the forward and backward branches, whereas the pulse experiment reports whether incomplete recovery between successive stimuli drives the state cumulatively upward or downward. Once θ is fixed, both observables inherit a definite sign when projected onto the measured drain current. This is also why the main text can summarize the CKW/CCW and potentiation/depression correspondence only after the polarity convention and pulse waveform have been specified.

In addition, the effective timescales used in the reduced model can be connected to experimental observables. The ionic relaxation time τ_d, defined in eq (1), describes the delayed approach of the internal state A toward the gate-defined equilibrium state A_{eq}. In experiments, τd can be estimated from film thickness and independently determined ionic diffusivity or extracted as an effective relaxation time from gate-current transients, chronoamperometry, electrochemical impedance spectroscopy, or thickness-dependent charging measurements. In a step experiment, τd controls the characteristic recovery of A toward A_{eq}; in frequency-domain measurements, it corresponds to the characteristic ionic relaxation frequency within the selected operating window.

The electronic readout time τ_e, defined in eq (2), describes how the channel state is projected into the measured drain current through lateral electronic transport. It can be estimated from device geometry, drain bias, and mobility or channel-transport measurements or obtained as an effective fitting parameter from drain-current transients or transfer-hysteresis data when the same current expression is used to describe the readout dynamics.

These estimates should be understood as operating-window descriptors rather than universal material constants. In real OECTs, ionic diffusivity, carrier mobility, chemical capacitance, carrier density, and channel conductivity may vary with gate bias, drain bias, and doping state. Therefore, the τ_d and τ_e are used in the simulations represent effective values over the selected bias window. The independent scans of τ_d and τ_e, in the main text, are used to identify response regimes of the reduced model. Experimentally, such tuning is approximate: τ_d may be modified by film thickness, ion species, electrolyte composition, swelling, and morphology, whereas τe may be

https://doi.org/10.1021/acsaelm.6c00658
ACS Appl. Electron. Mater. 2026, 8, 5453−5463

modified by channel length, drain bias, carrier mobility, carrier density, and contact/channel resistance.

APPENDIX 2. EXPERIMENTAL AND COMPUTATIONAL METHODS

Representative pulse measurements were carried out on n-PBDF OECTs to illustrate the operating-condition dependence of the apparent pulse-update polarity. The n-PBDF polymer was prepared following the reported synthesis of n-doped poly(benzodifurandione). The device fabrication followed a similar solution-processed OECT procedure, with the following modifications: the channel length was 50 μm, the n-PBDF film was deposited by spin coating at 2000 rpm, vacuum annealing at 50 °C overnight, and 0.1 M NaCl aqueous solution was used as the electrolyte.[12]

The numerical simulations were performed in MATLAB using the reduced state equation and drain current expression described in Appendix 1. The internal state A was evolved under either a linear gate-voltage sweep or a piecewise-constant pulse train. For pulse simulations, the gate voltage alternated between a baseline voltage and a pulse voltage. The resulting drain current was calculated from the same reduced current expression used in the main text.

For the transfer curve simulations, the gate voltage was swept forward and backward at the stated sweep rate, and the corresponding drain current was calculated to determine the CKW/CCW loop orientation. For the pulse-protocol simulations, the readout current was sampled at the same fixed point within each pulse, typically at the end of the pulse-on period, and potentiation/depression was inferred from the pulse-to-pulse evolution of the readout current magnitude.

ASSOCIATED CONTENT

Data Availability Statement

The simulation code and data presented here can be accessed at https://doi.org/10.5281/zenodo.19029528 (Zenodo) under the license CC BY 4.0 (Creative Commons Attribution 4.0 International).

Supporting Information

The Supporting Information is available free of charge at https://pubs.acs.org/doi/10.1021/acsaelm.6c00658.

Additional simulation results of long-interval pulse responses, drain-current comparisons under different operating conditions, and effective ionic-timescale variation studies (DOCX)

AUTHOR INFORMATION

Corresponding Authors

Heyi Zhang – *Instituto de Tecnología Química (ITQ), Consejo Superior de Investigaciones Científicas-Universitat Politècnica de València, 46022 Valencia, Spain; Institute of Advanced Materials (INAM), Universitat Jaume I, 12006 Castelló, Spain;* orcid.org/0000-0003-0443-3367; Email: hzhan12h@itq.upv.es

Juan Bisquert – *Instituto de Tecnología Química (ITQ), Consejo Superior de Investigaciones Científicas-Universitat Politècnica de València, 46022 Valencia, Spain;* orcid.org/0000-0003-4987-4887; Email: jbisquer@itq.upv.es

Author

Gonzalo Rivera-Sierra – *Instituto de Tecnología Química (ITQ), Consejo Superior de Investigaciones Científicas-Universitat Politècnica de València, 46022 Valencia, Spain;* orcid.org/0009-0008-2651-9157

Complete contact information is available at: https://pubs.acs.org/doi/10.1021/acsaelm.6c00658

Notes

The authors declare no competing financial interest.

ACKNOWLEDGMENTS

The work was funded by the European Research Council (ERC) via Horizon Europe Advanced Grant, grant agreement n^0 101097688 ("PeroSpiker"). Additional institutional support by the Spanish Ministry of Science and Innovation (CEX2021-001230-S grant funded by MCIN/AEI/10.13039/501100011033) is gratefully acknowledged. Funding for open access charge: CRUE-Universitat Politècnica de València.

REFERENCES

(1) Friedlein, J. T.; McLeod, R. R.; Rivnay, J. Device physics of organic electrochemical transistors. *Org. Electron.* **2018**, *63*, 398–414.

(2) Kim, H.; Won, Y.; Song, H. W.; Kwon, Y.; Jun, M.; Oh, J. H. Organic Mixed Ionic-Electronic Conductors for Bioelectronic Sensors: Materials and Operation Mechanisms. *Adv. Sci. (Weinh)* **2024**, *11*, e2306191.

(3) Kim, Y.; Kimpel, J.; Giovannitti, A.; Muller, C. Small signal analysis for the characterization of organic electrochemical transistors. *Nat. Commun.* **2024**, *15*, 7606.

(4) Kukhta, N. A.; Marks, A.; Luscombe, C. K. Molecular Design Strategies toward Improvement of Charge Injection and Ionic Conduction in Organic Mixed Ionic-Electronic Conductors for Organic Electrochemical Transistors. *Chem. Rev.* **2022**, *122*, 4325–4355.

(5) Ohayon, D.; Druet, V.; Inal, S. A guide for the characterization of organic electrochemical transistors and channel materials. *Chem. Soc. Rev.* **2023**, *52*, 1001–1023.

(6) Qin, S.; Sun, Z.; Li, H.; Rahman, C.; Gartner, T. E., 3rd; Reichmanis, E. Organic Mixed Ionic-Electronic Conductors for Organic Electrochemical Transistors: Sidechain Structure Influences Ion Uptake and Functional Performance. *ChemPhysChem* **2025**, *26*, e202500403.

(7) Rivnay, J.; Inal, S.; Salleo, A.; Owens, R. M.; Berggren, M.; Malliaras, G. G. Organic electrochemical transistors. *Nat. Rev. Mater.* **2018**, *3*, 17086.

(8) Gkoupidenis, P.; Schaefer, N.; Garlan, B.; Malliaras, G. G. Neuromorphic Functions in PEDOT:PSS Organic Electrochemical Transistors. *Adv. Mater.* **2015**, *27*, 7176–7180.

(9) Gkoupidenis, P.; Schaefer, N.; Strakosas, X.; Fairfield, J. A.; Malliaras, G. G. Synaptic plasticity functions in an organic electrochemical transistor. *Appl. Phys. Lett.* **2015**, *107*, 263302.

(10) Wang, S.; Chen, X.; Zhao, C.; Kong, Y.; Lin, B.; Wu, Y.; Bi, Z.; Xuan, Z.; Li, T.; Li, Y.; Zhang, W.; Ma, E.; Wang, Z.; Ma, W. An organic electrochemical transistor for multi-modal sensing, memory and processing. *Nat. Electron.* **2023**, *6*, 281–291.

(11) Burgt, Y., van de; Lubberman, E.; Fuller, E. J.; Keene, S. T.; Faria, G. C.; Agarwal, S.; Marinella, M. J.; Alec Talin, A.; Salleo, A. A non-volatile organic electrochemical device as a low-voltage artificial synapse for neuromorphic computing. *Nat. Mater.* **2017**, *16*, 414–418.

(12) Sanjuan, I.; Franco, D.; Chen, Q. G.; Chueh, C. C.; Lee, W. Y.; Guerrero, A. Proton Migration-Modulated n-Doped Poly(benzodifurandione) Organic Electrochemical Transistors Used

for Neuromorphic Computing Applications. *ACS Energy Lett.* **2025**, *10*, 5209–5217.
(13) Shu, H.; Long, H.; Sun, H.; Li, B.; Zhang, H.; Wang, X. Dynamic Model of the Short-Term Synaptic Behaviors of PEDOT-based Organic Electrochemical Transistors with Modified Shockley Equations. *ACS Omega* **2022**, *7*, 14622–14629.
(14) Xu, C.; Gao, L.; Peng, Y.; Liu, C.; Zheng, D.; Yu, J. Ionic-Electronic Coupling Modulation Induced by Nanofibrous Phase Separation for Synaptic Organic Electrochemical Transistors. *Aggregate* **2025**, *6*, e70129.
(15) Bisquert, J. Hysteresis in Organic Electrochemical Transistors: Distinction of Capacitive and Inductive Effects. *J. Phys. Chem. Lett.* **2023**, *14*, 10951–10958.
(16) Bisquert, J.; Ilyassov, B.; Tessler, N. Switching Response in Organic Electrochemical Transistors by Ionic Diffusion and Electronic Transport. *Adv. Sci. (Weinh)* **2024**, *11*, e2404182.
(17) Kumar, R.; Luginieski, M.; Kumar, A.; Barbosa, H. F. d. P.; Schander, A.; Faria, G. C.; Lüssem, B. Regular and Inverted Hysteresis in Organic Electrochemical Transistors: Mechanisms and Electrochemical Insights. *Adv. Electron. Mater.* **2025**, *11*, e00176.
(18) Mariani, F.; Decataldo, F.; Bonafe, F.; Tessarolo, M.; Cramer, T.; Gualandi, I.; Fraboni, B.; Scavetta, E. High-Endurance Long-Term Potentiation in Neuromorphic Organic Electrochemical Transistors by PEDOT:PSS Electrochemical Polymerization on the Gate Electrode. *ACS Appl. Mater. Interfaces.* **2024**, *16*, 61446–61456.
(19) Song, S. H.; Song, J. H.; Park, J.; Yoo, H.; Lee, E. K. Improved neuromorphic functionality in organic electrochemical transistors using crosslinked-polyvinyl alcohol for fast ion transport and its application to Pavlovian transistors. *J. Mater. Chem. C* **2025**, *13*, 16657–16666.
(20) Xiang, C.; Jiang, X.; Li, B.; Jiang, J.; Wang, Q.; Shi, C.; Dong, X.; Liu, D.; Xue, D.; Zhang, J.; Huang, L.; Chi, L. Thermal Annealing-modulated Ion Doping and Synaptic Behavior of Organic Electrochemical Transistors Based on Block Copolymers. *Chem. Res. Chin. Univ.* **2025**, *41*, 1037–1047.
(21) Wan, X.; Yan, J.; Cui, S.; Xu, Y.; Huabin, S. An ion-modulated organic electrochemical synaptic transistor for efficient parallel computing and in-situ training. *Org. Electron.* **2025**, *143*, 107253.
(22) Bernards, D. A.; Malliaras, G. G. Steady-State and Transient Behavior of Organic Electrochemical Transistors. *Adv. Funct. Mater.* **2007**, *17*, 3538–3544.
(23) Nissa, J.; Janson, P.; Berggren, M.; Simon, D. T. The Role of Relative Capacitances in Impedance Sensing with Organic Electrochemical Transistors. *Adv. Electron. Mater.* **2021**, *7*, 2001173.
(24) Bisquert, J.; Tessler, N. Transient Current Responses of Organic Electrochemical Transistors: Evaluating Ion Diffusion, Chemical Capacitance, and Series Elements. *Adv. Funct. Mater.* **2024**, *35*, 2419000.
(25) Zhang, H.; Bisquert, J. Gate-voltage-dependent ionic diffusion and transient dynamics in organic electrochemical transistors. *Org. Electron.* **2026**, *149*, 107367.
(26) Bisquert, J.; Keene, S. T. Using the Transversal Admittance to Understand Organic Electrochemical Transistors. *Adv Sci (Weinh)* **2025**, *12*, e2410393.
(27) Xiang, K.; Song, J.; Liu, H.; Chen, J.; Yan, F. Organic Electrochemical Transistors for Neuromorphic Devices and Applications. *Adv. Mater.* **2026**, *38*, e15532.
(28) Rashid, R. B.; Ji, X.; Rivnay, J. Organic electrochemical transistors in bioelectronic circuits. *Biosens. Bioelectron.* **2021**, *190*, 113461.
(29) Park, S. M.; Won, Y.; Oh, J. H.; Lee, E. K. Enhancement of Synaptic Behavior in Organic Electrochemical Transistors via the Introduction of Layer-by-Layer Grown Metal-Organic Framework. *Adv. Mater. Technol.* **2024**, *10*, 2401316.
(30) Wang, Z.; Yan, F. Organic Transistor-Based Neuromorphic Electronics and Their Recent Applications. *Small Methods* **2026**, *10*, e01966.
(31) Ji, X.; Paulsen, B. D.; Chik, G. K. K.; Wu, R.; Yin, Y.; Chan, P. K. L.; Rivnay, J. Mimicking associative learning using an ion-trapping non-volatile synaptic organic electrochemical transistor. *Nat. Commun.* **2021**, *12*, 2480.
(32) Niu, X.; Wang, Z.; Wang, M.; Yao, J.; Chai, X.; Ji, J.; Sang, S. A testable weighting factor for accurate analysis of the organic electrochemical transistors' transient response behavior. *J. Appl. Phys.* **2025**, *137*, 115501.

https://doi.org/10.1021/acsaelm.6c00658
ACS Appl. Electron. Mater. 2026, 8, 5453–5463